Monthly Notices of the ROYAL ASTRONOMICAL SOCIETY

MNRAS **513,** 6074–6087 (2022) https://doi.org/10.1093/mnras/stac1289
Advance Access publication 2022 May 10

Understanding the physical state of hot plasma formed through stellar wind collision in WR140 using high-resolution X-ray spectroscopy

Asca Miyamoto,[1★] Yasuharu Sugawara,[2] Yoshitomo Maeda,[2★] Manabu Ishida,[1,2★] Kenji Hamaguchi,[3,4] Michael Corcoran,[3] Christopher M. P. Russell[5] and Anthony F. J. Moffat[6]

[1] *Department of Physics, Tokyo Metropolitan University, 1-1 Minami-Osawa, Tokyo 192-0397, Japan*
[2] *The Institute of Space and Astronautical Science/JAXA, 3-1-1 Yoshinodai, Chuo-ward, Sagamihara, Kanagawa 252-5210, Japan*
[3] *CRESST II and X-ray Astrophysics Laboratory NASA/GSFC, Greenbelt, MD 20771, USA*
[4] *Department of Physics, University of Maryland, Baltimore County, 1000 Hilltop Circle, Baltimore, MD 21250, USA*
[5] *Department of Physics and Astronomy, Bartol Research Institute, University of Delaware, Newark, DE 19716 USA*
[6] *Département de physique and Centre de Recherche en Astrophysique du Québec (CRAQ), Université de Montréal, CP 6128, Montréal, Canada*

Accepted 2022 May 1. Received 2022 April 28; in original form 2022 March 24

ABSTRACT

We analyse a series of *XMM–Newton* RGS data of the binary Wolf–Rayet star WR140 that encompasses one entire orbit. We find that the RGS detects X-rays from optically thin thermal plasma only during orbital phases when the companion O star is on the near side of the WR star. Although such X-rays are believed to be emitted from the shock cone formed through collision of the stellar winds, temperature and density profiles of the plasma along the cone have not been measured observationally. We find that the temperature of the plasma producing Ne emission lines is 0.4–0.8 keV, using the intensity ratio of Kα lines from He-like and H-like Ne. We also find, at orbital phases 0.816 and 0.912, that the electron number density in the Ne line-emission site is approximately 10^{12} cm^{-3} from the observed intensity ratios *f*/*r* and *i*/*r* of the He-like triplet. We calculated the shock cone shape analytically, and identify the distance of the Ne line-emission site from the shock stagnation point to be 0.9–8.9 $\times$ 10^{13} cm using the observed ratio of the line-of-sight velocity and its dispersion. This means that we will be able to obtain the temperature and density profiles along the shock cone with emission lines from other elements. We find that the photoexcitation rate by the O star is only 1.3–16.4 per cent of that of the collisional excitation at orbital phase 0.816. This implies that our assumption that the plasma is collisionally excited is reasonable, at least at this orbital phase.

Key words: stars: winds, outflows – stars: Wolf–Rayet – X-rays: stars.

1 INTRODUCTION

A classical Wolf–Rayet star (WR star) is the last stage of evolution of a massive star with an initial main-sequence mass of $\gtrsim 25\,M_{\odot}$. Its high optical luminosity, more than $10^5\,L_{\odot}$, is maintained by He-burning in the central core. The WR star is classified into WN, WC, or WO subtypes, which are characterized by highly ionized broad nitrogen, carbon, and oxygen lines, respectively, in addition to He-lines. In general, WR stars have stellar winds with large mass-loss rates, often more than $10^{-5}\,M_{\odot}\,\mathrm{yr}^{-1}$, and wind speeds as high as a few times 1000 km s^{-1}.

WR140 (HD193793), the subject of this paper, is a binary composed of a WR star and an O star whose spectral types are WC7pd and O5.5fc, respectively (Fahed et al. 2011), orbiting each other with a period of $\simeq$8 yr. Orbital parameters of the WR140 binary that we adopt in this paper are summarized in Table 1, which are measured by Monnier et al. (2011) using high-resolution near-infrared interferometers (more recent parameters are measured by Thomas et al. 2021. The orbit of WR140 is highly eccentric with $e = 0.8964$. The inclination implies that the component stars execute a retrograde (clock wise) motion on the celestial sphere. The orbit viewed from the earth is sketched in fig. 1 of Monnier et al. 2011).

Like other WR binaries, the WR140 binary is also characterized by large mass-loss associated with high-velocity stellar winds from each component star. From a series of *Suzaku* observations, Sugawara et al. (2015) calculated $\dot{M} = 2.2 \times 10^{-5}\,M_{\odot}\,\mathrm{yr}^{-1}$ for the WR star. Based on the orbital-phase-dependent X-ray intensity variation, they also derived $9 \times 10^{-7}\,M_{\odot}\,\mathrm{yr}^{-1}$ from the O star (see also Pittard & Dougherty 2006; Fahed et al. 2011). Radiatively driven stellar winds accelerate according to a standard velocity law

$$v(r) = v_{\infty}\left(1 - \frac{R_*}{r}\right)^{\beta}, \quad (1)$$

where v_{∞} is the terminal velocity of the wind, which is 2860 km s^{-1} for the WR star (Williams et al. 1990) and 3100 km s^{-1} for the O star (Setia Gunawan et al. 2001), R_* is the radius of the star which is 2 and 26 $R_{\odot}$ for the WR star (hydrostatic core) and the O star, respectively (Williams et al. 2009), and $\beta \simeq 1$ for the O star whereas $\beta > 1$ for the WR star (Puls et al. 1996; Lépine & Moffat 1999). In the WR140 binary, these strong stellar winds collide with each other and form a shock cone around the O star. X-ray emission emanates from a plasma which is compressed and is heated up in the shock. X-ray

★ E-mail: miyamoto-asuka@ed.tmu.ac.jp (AM); ymaeda@astro.isas.jaxa.jp (YM); ishida@astro.isas.jaxa.jp (MI)

Table 1. Ortibal parameters of WR140 (Monnier et al. 2011).

Parameter	Value
a (au)	15.3
e	0.8964
i (°)	119.6
Ω (°)	353.6
ω (°)	46.8
T_0 (MJD)	46154.8
P (d)	2896.35

emission from WR140 has been studied previously (Koyama et al. 1990, 1994; Zhekov & Skinner 2000; Pollock et al. 2005; De Becker et al. 2011; Sugawara et al. 2015; Pollock et al. 2021) using data from many individual X-ray observatories. Sugawara et al. (2015) used a total of four *Suzaku* observations of WR140 from 2008 April through 2009 January, which sampled orbital phases between 0.90 and 1.00. They detected a high-temperature optically thin thermal plasma component whose temperature is between 3.0–3.5 keV from all the four observations, and moderate temperature (kT = 0.4–0.7 keV) and low-temperature (kT = 21 eV) components from the first two orbital phases, 0.904 and 0.989. The high-temperature component probably originates near the stagnation point, the region where the winds collide head-on, where the plasma heating is taking place most efficiently. The low-temperature component, on the other hand, shows characteristics of a recombining plasma, suggesting that it is of a cooling plasma origin and is emitted from the shock cone far downstream from the stagnation point. Pollock et al. (2005) examined He-like and H-like K lines from O to Fe, and Fe L lines in high-resolution grating observations with the *Chandra* HETG at orbital phases 0.987 and 0.032 to examine flow velocities, ionization structure and elemental abundance in the hot shocked gas.

In this paper, we present our analysis of the X-ray-emitting hot plasma in the colliding shock using the Reflection Grating Spectrometer (RGS, den Herder et al. 2001) onboard *XMM–Newton* (Jansen et al. 2001). The paper is organized as follows. In Section 2, we list the data that are used in this paper and describe the data reduction. In Section 3, we explain data analysis methods, goals, and results in an attempt to understand the geometry and distribution of temperature and density of the plasma along the shock cone using density diagnostics from the Ne IX He-like triplet (Porquet et al. 2001, and references therein). In Section 4, we calculate the geometry of the shock cone under the assumption of pressure balance between the winds from the two stellar components, and discuss the location and state of the plasma that emits the Ne He-like triplet. In Section 5, we summarize our results.

2 OBSERVATIONS

We use data from the RGS onboard *XMM–Newton* for our analysis. The RGS consists of a reflective-grating spectrograph that disperses X-rays collected by the mirror. The X-rays are finally detected with a CCD array, with their energies being assigned from the positions on the array. The RGS covers an energy range of about 0.33–2.5 keV.

We analyse 12 observations obtained by *XMM–Newton* from May 2008 to June 2016, which cover one entire orbit of WR140. The observation log, including the observation start time, the exposure time, and the orbital phase is summarized in Table 2. Each data set is labelled from A (0.912) to L (0.935). The mean and true anomalies and the distance between the two-component stars of each data set are summarized in Table 3. Pollock et al. (2021) found from their extensive analysis of data from *RXTE*, *Swift* XRT, and *NICER* taken over ∼20 yr that there is little orbit-to-orbit difference in X-ray behaviour of WR140. Hence, our full orbit data set can be regarded as generally representative of the X-ray emission from WR140.

Fig. 1 shows the orbit of the O star with respect to the WR star, viewed from the direction perpendicular to the orbital plane. The blue and red parts of the orbit indicate the O star positions which are closer to or farther away from the observer than the WR star, respectively. The O star is closer to the observer than the WR star in all the data sets except F (0.029) and G (0.031).

3 DATA ANALYSIS AND RESULTS

3.1 Data reduction

For the data analysis, we use the HEASOFT software version 6.27.2[1] provided by NASA's Goddard Space Flight Center and the SAS version 19.1.0[2] with the Current Calibration Files (CCF) provided by ESA. In addition, we use the XSPEC version 12.11.0 (Arnaud 1996) to display and evaluate the spectra. First, we create event files of the first order and second order dispersions of the RGS1 and RGS2 separately. Then we derive source and background spectra from them, and build response files. These data reductions are carried out with the SAS software version 19.1.0, according to standard procedures.

Fig. 2 shows all the spectra analyzed here. The two brightest spectra are from phase B (0.968), followed by phase L (0.935). We note that the inferior conjunction of the O star is between these two phases. We also find that WR140 is hardly detected in observations E (0.994), F (0.029), and G (0.031). Of these, the O star is on the far side of the WR star in the latter two phases, and WR140 is detected mainly at phases when the O star is in front. This indicates that the pre-shock stellar wind from the WR star is so dense that the X-rays in the RGS band ($\lesssim$2 keV) cannot penetrate it and reach the observer. Sugawara et al. (2015) observed WR140 in the same orbit as our observations and found that the flux below 2 keV almost disappeared between the orbital phases 0.989 and 0.997, which are close to our phase D (0.987) and phase E (0.994). In the following analysis, we will use the five brightest data sets K (0.816), A (0.912), L (0.935), B (0.968), and D (0.987). Pollock et al. (2005) made high-resolution observations by the *Chandra* HETG in WR140 at orbital phases 0.987 and 0.032. The orbital phase 0.987, which is 0.986 in the ephemeris we use, is very close to our phase D (0.987), hence we can compare them directly. On the other hand, the HETG intensity at phase 0.032 dropped to about 1/10 of the intensity at phase 0.987, which is too faint for any useful comparison.

3.2 Phase resolved spectra

We evaluated the spectra shown in Fig. 2 by model fitting with XSPEC. In doing this, we adopted the models bvapec and tbabs. Bvapec is a model describing an X-ray emission spectrum from an optically thin thermal plasma in collisional ionization equilibrium. It is calculated from the AtomDB atomic database,[3] along with a plasma temperature, abundances of He, C, N, O, Ne, Mg, Al, Si, S, Ar, Ca, Fe, Ni with reference to Solar, a redshift, a Gaussian sigma for velocity broadening of the emission lines, and a normalization, all

[1] https://heasarc.gsfc.nasa.gov/docs/software/lheasoft/
[2] https://www.cosmos.esa.int/web/xmm-newton/sas
[3] http://www.atomdb.org/index.php

Table 2. Observation log of WR140. Intensity is the count rate from the first-order spectrum of RGS1.

Reference number	Observation ID	Observation start (UT)	Exposure (s)	Orbital phase	Intensity (count s^{-1})
0555470701	A	2008/05/02 19:34	22 913	0.912	0.304
0555470801	B	2008/10/11 11:31	23 415	0.968	0.378
0555470901	D	2008/12/05 20:28	36 069	0.987	0.238
0555471001	E	2008/12/26 00:01	26 915	0.994	0.004
0555471101	F	2009/04/06 19:45	24 919	0.029	0.009
0555471201	G	2009/04/12 15:32	22 915	0.031	0.012
0651300301	H	2010/05/08 21:53	22 919	0.166	0.088
0651300401	J	2011/04/06 09:45	29 915	0.281	0.095
0762910301	K	2015/07/02 15:18	29 638	0.816	0.201
0784130301	L	2016/06/13 20:53	18 900	0.935	0.322

Table 3. Distance between the component stars (d), mean and true anomalies M and θ.

Observation ID	d (au)	M (°)	θ (°)
A	13.54	328.3	209.8
B	6.85	348.5	231.2
D	3.61	355.3	259.1
E	2.27	357.8	291.2
F	6.39	10.4	126.2
G	6.70	11.2	128.0
H	19.65	59.8	160.9
J	25.25	101.2	169.4
K	20.74	293.8	197.5
L	11.14	336.6	215.5

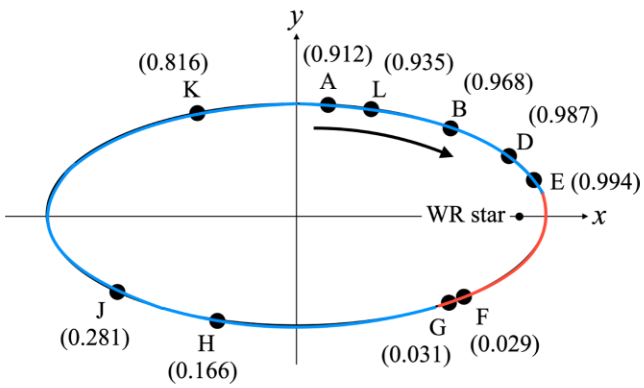

Figure 1. The orbit of the O star viewed from the direction perpendicular to the binary orbital plane with the WR star being fixed at one of the foci. The number in parentheses indicates the orbital phase of each data set. The blue and red parts of the orbit mean that the O star is in the foreground, and in the background of the WR star, respectively.

of which can be set as parameters. We adopted Anders & Grevesse (1989) as to the reference solar abundance. Tbabs is a model that calculates the cross-section of X-ray photoelectric absorption as the sum of that of the gas-phase ISM, the particle-phase ISM, and the molecules in the ISM, and an equivalent hydrogen column density can be set as a parameter for fitting.

In Fig. 3, we show the spectrum of the data set A (0.912), as an example. We identify the elements and their ionization states of intense emission lines using the AtomDB atomic database. The spectrum is composed mainly of neon and oxygen K lines and iron L lines. With the model described above, we carried out spectral fitting for the spectra at phase K (0.816), A (0.912), L (0.935), B (0.968), and D (0.987) separately. The best-fitting model is overlaid in Fig. 3 for phase A (0.912), and the best-fitting parameters for all five phases are summarized in Table 4. Hydrogen column densities at all these phases are measured to be 6–7 $\times$ 10^{21} cm^{-2}. This value is consistent with that measured with the *Swift* XRT, 5-10 $\times$ 10^{21} cm^{-2} during the period of -150 to -40 d from the periastron (Pollock et al. 2021).

We adopt C-statistics for evaluation of the spectral fit quality throughout this paper. The errors quoted are always at the 90 per cent confidence level.

3.3 Radial velocity and velocity dispersion of Ne

Among a number of emission lines, those from Ne are particularly strong. We therefore attempted to carry out a plasma diagnosis with the Ne IX and Ne X lines. The spectra of the Ne Kα lines at phase A (0.912) from RGS1 and RGS2 are shown in Fig. 4. The He-like triplet is composed of a forbidden line (z), intercombination lines (x and y), and a resonance line (w), which are marginally resolved by the RGS, because of limited statistics and energy resolution, and line broadening as well. The line-of-sight velocity and velocity dispersion for the data sets A (0.912), B (0.968), D (0.987), K (0.816), and L (0.935), and the best-fitting parameters are summarized in Table 5. One of the *Chandra* HETG observations (Pollock et al. 2005) corresponds to orbital phase 0.986 in our ephemeris, which is between phase B (0.968) and phase D (0.987). Correspondingly, the velocity of the Ne-Kα line obtained by *Chandra* at this phase is -630 km s^{-1} $< v_{los} <$ -620 km s^{-1}, which is close to our velocity -622 km s^{-1} (Table 5) at phase D (0.987). Also the HETG velocity width is 414 km s^{-1} $< \sigma_{los} <$ 431 km s^{-1}, which is close to our phase B (0.968) (420 km s^{-1}, see Table 5). The temperatures summarized in Table 5 are the ionization temperature of Ne, and can be regarded as the temperatures near the Ne line-emission region. The line-of-sight velocity (v_{los}) and the velocity dispersion (σ_{los}) in this Table are plotted in Fig. 5 as a function of the orbital phase. The line-of-sight velocity is negative at all phases, with a maximum blue shift of about 1200 km s^{-1}, which is consistent with an interpretation in which the plasma flows from the stagnation point towards the O star, which locates closer to the observer than the WR star. The velocity dispersion ranges 470–700 km s^{-1}. Using observed v_{los} and σ_{los}, we will identify the Ne line-emission site along the colliding shock cone in Section 4.1.

3.4 Density diagnosis by the He-like triplet of Ne

As mentioned in Section 3.3, we marginally resolved the He-like triplet emission lines of Ne. A number of previous works (Gabriel & Jordan 1969; Pradhan & Shull 1981; Porquet et al. 2001) pointed

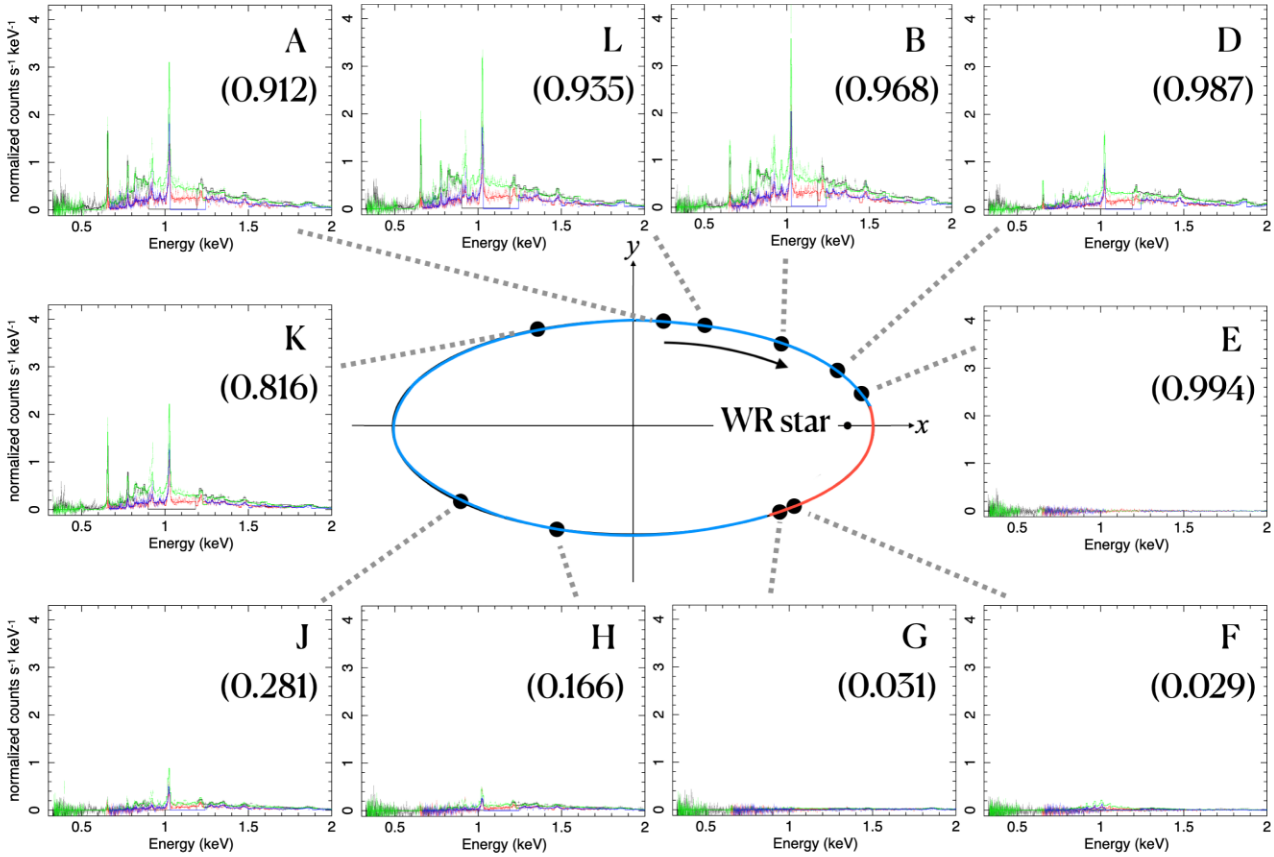

Figure 2. The ensemble of the spectra from all phases. The numbers in parentheses indicate the orbital phases (Table 2). WR140 is detected mainly at phases K (0.816), A (0.912), L (0.935), B (0.968), and D (0.987), when the O star is in front, whereas it is hardly detected at the phases F (0.029) and G (0.031) when the O star is on the far side of the WR star (and at phase E (0.994)).

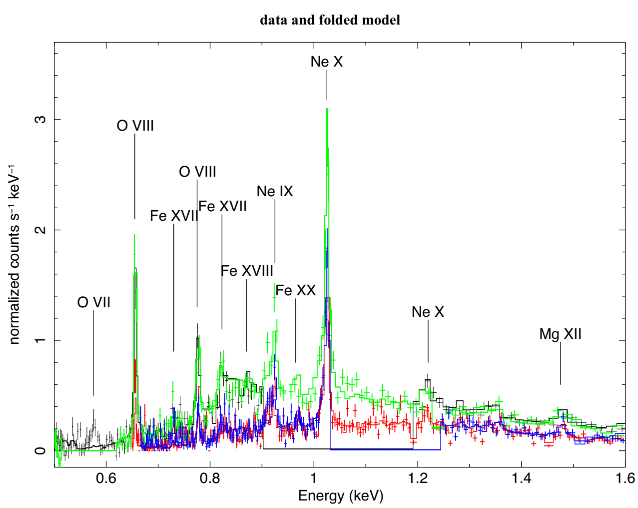

Figure 3. The spectrum of phase A (0.912) as an example, with the best-fitting models being overlaid as histograms. Black, red, green, and blue represent the data and the model of the first orders of the RGS1 and RGS2, and the second orders of the RGS1 and RGS2, respectively. Some data gaps, depending upon detectors and/or orders, exist because the corresponding area of the detector is broken. We identified the elements and their ionization states of intense emission lines with the AtomDB atomic database. Ne and O K lines and Fe L lines dominate the spectra. The best-fitting parameters are summarized in Table 4.

out that the intensity ratio of $i = x + y$ and z is sensitive to plasma electron density. This is because the upper level of z ($^3S_1$) has a relatively long lifetime and it can be excited again to the upper level of x and y ($^3P_{1,2}$) by an electron impact in the plasma. We therefore evaluated the intensities of the He-like triplet components of Ne as follows.

First we adopted the best-fitting parameters of the spectral fits in the band 0.5–1.6 keV from Table 4, but isolate the He-like Ne emission lines, and perform a new model fitting with bvapec and tbabs. We included three redshifted gaussians (zgauss) to the region around the Ne IX triplet, allowing the line redshift to vary and using a tbabs∗bvapec model with the Ne abundance set to zero as our estimate of the continuum near the triplet. As shown in Fig. 4, however, these three line components are resolved only marginally. Hence, we assumed that each component of the triplet had the same velocity, and linked the line central energies of the intercombination and resonance lines to that of the forbidden line, according to the ratios of their rest-frame energies, which are 0.9050, 0.9148, and 0.9220 keV for the forbidden, intercombination and resonance components, respectively. The line central energies of the zgauss models are fixed at these values, and they are effectively floated with the redshift parameter z that is common among all the line components. The sigma parameter of the forbidden line σ_f is allowed to vary, and that of the other two lines are linked to σ_f multiplied by their respective central energy ratios, as is the case for the line central energies. In the course of our analysis, we find that the redshift z is not constrained very well solely with the He-like emission line. Hence,

Table 4. Best-fitting parameters of the model composed of the bvapec model multiplied by the photoelectric absorption model tbabs applied to the spectra at the phases K (0.816), A (0.912), L (0.935), B (0.968), and D (0.987) in the band 0.6–1.6 keV (Fig. 3). kT is a plasma temperature, $Z_{\rm element}$ are abundances with reference to Solar based on Anders & Grevesse (1989). $v_{\rm los}$ is a line-of-sight velocity. $\sigma_{\rm los}$ is a Gaussian sigma associated with velocity broadening of the lines. Norm. implies a normalization of the model, which is an emission measure divided by the distance squared. $N_{\rm H}$ is a hydrogen column density to the plasma. $N_{\rm H}$ is an equivalent hydrogen column density. C-statistics (dof) is the total fit statistic.

ID Phase	K 0.816	A 0.912	L 0.935	B 0.968	D 0.987
kT (keV)	$0.793^{+0.021}_{-0.017}$	$0.799^{+0.034}_{-0.017}$	$0.786^{+0.015}_{-0.018}$	$0.842^{+0.029}_{-0.013}$	$1.514^{+0.162}_{-0.063}$
$Z_{\rm O}$	$1.062^{+0.156}_{-0.105}$	$0.871^{+0.133}_{-0.100}$	$0.848^{+0.136}_{-0.097}$	$0.984^{+0.170}_{-0.104}$	$0.975^{+0.212}_{-0.117}$
$Z_{\rm Ne}$	$0.775^{+0.078}_{-0.054}$	$0.624^{+0.077}_{-0.047}$	$0.598^{+0.060}_{-0.044}$	$0.679^{+0.067}_{-0.038}$	$1.206^{+0.308}_{-0.130}$
$Z_{\rm Mg}$	$0.133^{+0.027}_{-0.022}$	$0.117^{+0.030}_{-0.016}$	$0.130^{+0.023}_{-0.016}$	$0.138^{+0.024}_{-0.019}$	$0.321^{+0.091}_{-0.048}$
$Z_{\rm Si}$	$0.131^{+0.028}_{-0.021}$	$0.140^{+0.027}_{-0.024}$	$0.146^{+0.027}_{-0.019}$	$0.122^{+0.024}_{-0.019}$	$0.674^{+0.169}_{-0.067}$
$Z_{\rm Fe} = Z_{\rm Ni}$	$0.050^{+0.008}_{-0.005}$	$0.041^{+0.007}_{-0.004}$	$0.045^{+0.006}_{-0.005}$	$0.061^{+0.008}_{-0.005}$	$0.013^{+0.008}_{-0.006}$
$v_{\rm los}$ (10^3 km s^{-1})	$-1.156^{+0.055}_{-0.054}$	$-1.108^{+0.022}_{-0.055}$	$-1.276^{+0.049}_{-0.046}$	$-1.184^{+0.032}_{-0.036}$	$-0.645^{+0.055}_{-0.076}$
$\sigma_{\rm los}$ (km s^{-1})	$698.6^{+70.1}_{-49.9}$	$529.9^{+61.7}_{-72.7}$	$533.8^{+67.1}_{-68.5}$	$467.5^{+73.6}_{-71.5}$	$539.9^{+100.0}_{-70.2}$
Norm. ($10^{-14}/4\pi\,$cm^{-5})	$0.086^{+0.004}_{-0.005}$	$0.140^{+0.007}_{-0.011}$	$0.160^{+0.006}_{-0.008}$	$0.192^{+0.007}_{-0.012}$	$0.092^{+0.003}_{-0.007}$
$N_{\rm H}$ (10^{22} cm^{-2})	$0.585^{+0.020}_{-0.014}$	$0.590^{+0.020}_{-0.023}$	$0.626^{+0.018}_{-0.017}$	$0.696^{+0.020}_{-0.021}$	$0.594^{+0.011}_{-0.019}$
C-statistics (dof)	11307.77 (11244)	11292.33 (11250)	10346.79 (11238)	11086.18 (11242)	12263.90 (11188)

the error of the redshift parameter is evaluated manually. We first fix the redshift z at the best-fitting value determined with the previous fitting including the H-like Ne line (Table 5), and the normalizations of the lines and $\sigma_{\rm f}$ are allowed to vary. We then perform the same fitting with the maximum and the minimum values of the redshift. We perform the same operation for the phases K (0.816), L (0.935), B (0.968), and D (0.987). The best-fitting parameters and spectra are shown in Table 6 and Fig. 6, respectively.

We will use these triplet intensities to estimate the electron density at all phases in Section 4.

4 DISCUSSION

4.1 Derivation of the shape of the shock cone and the Ne line-emission site

4.1.1 Overview

In order to understand the plasma profiles along the shock cone using the observed line-of-sight velocity $|v_{\rm los}|$ and its dispersion $\sigma_{\rm los}$ shown in Fig. 5, we first calculate the shape of the shock cone generated by the colliding stellar winds of WR140. The line-emitting plasma flows along the shock cone, and hence, it is possible to obtain an average orientation of the plasma flow and its velocity dispersion around the average velocity by calculating the shape of the shock cone. Assuming that the Ne line-emission site is axially symmetric, we can calculate the ratio of the line-of-sight velocity ($v_{\rm los}$) and its dispersion ($\sigma_{\rm los}$) by taking an azimuthal average of the orientation vector over the shock cone. It is thought that $|v_{\rm los}|$ increases whereas $\sigma_{\rm los}$ decreases monotonically along the shock cone as the distance from the stagnation point increases, after some simple calculations in Section 4.1.4. Consequently, the curve $|v_{\rm los}|/\sigma_{\rm los}$ is expected to increase monotonically (Fig. 9). By taking the ratio of the line-of-sight velocity and velocity dispersion of the observed data (Fig. 5), and comparing it with the theoretical curve, we can determine the location of the Ne emission site without complicated calculation of the absolute value of the plasma flow velocity along the shock cone.

Using the He-like triplet of Ne, we can estimate the electron number density of the Ne line-emission site, according to the principle described in Section 3.4. However, we may overestimate the density due to photoexcitation by extreme ultraviolet radiation from the O star (Section 4.2.2). Knowledge of the shock cone shape is of essential importance in evaluating the effect of the photoexcitation to the density calculation.

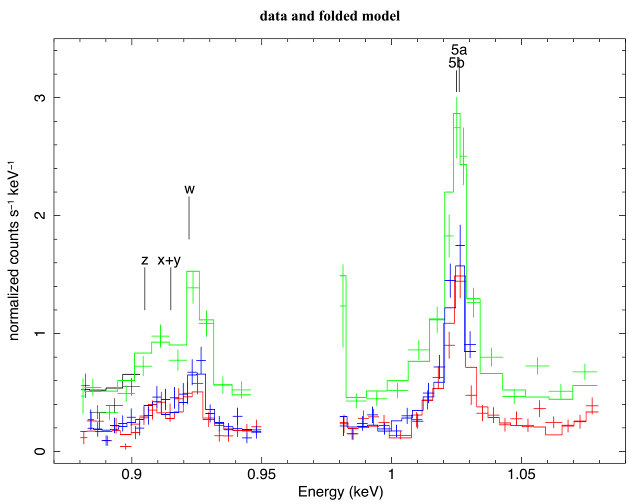

Figure 4. The spectrum of phase A (0.912) around energy bins of Kα lines of Ne X and Ne IX with the best-fitting bvapec and tbabs model being overlaid. The colour assignment of the data and the model are the same as those in Fig. 3. 5*a* and 5*b* indicate H-like resonance lines of Ne. w, $x + y$, and z are a resonance line, intercombination lines, and a forbidden line of He-like Ne, respectively. The best-fitting parameters are summarized in Table 5.

4.1.2 Location of the stagnation point

As the first step to deduce the overall shape of the shock cone, we calculate the location of its stagnation point. On the line connecting the centers of the WR star and the O star, the stellar winds undergo a simple head-on collision. Here, we neglect the effect of Coriolis force, because its effect is negligible at the phases before periastron

Table 5. Best-fitting parameters of the fit to the Kα lines of Ne X and Ne IX with the bvapec and tbabs models (Fig. 4). Parameters of abundances other than Ne and N_H are fixed at the best-fitting parameters in the band 0.5–1.6 keV (Table 4). The parameters kT, Z_{Ne}, v_{los}, σ_{los}, and normalization are allowed to vary.

ID Phase	K 0.816	A 0.912	L 0.935	B 0.968	D 0.987
kT (keV)	$0.453^{+0.017}_{-0.014}$	$0.474^{+0.021}_{-0.018}$	$0.469^{+0.024}_{-0.017}$	$0.839^{+0.029}_{-0.033}$	$0.584^{+0.063}_{-0.033}$
Z_O	1.062 (fixed)	0.871 (fixed)	0.848 (fixed)	0.984 (fixed)	0.975 (fixed)
Z_{Ne}	$0.277^{+0.032}_{-0.025}$	$0.255^{+0.032}_{-0.027}$	$0.216^{+0.029}_{-0.021}$	$0.604^{+0.062}_{-0.062}$	$0.278^{+0.062}_{-0.034}$
Z_{Mg}	0.133 (fixed)	0.117 (fixed)	0.130 (fixed)	0.138 (fixed)	0.320 (fixed)
Z_{Si}	0.131 (fixed)	0.140 (fixed)	0.146 (fixed)	0.122 (fixed)	0.673 (fixed)
$Z_{Fe} = Z_{Ni}$	0.050 (fixed)	0.041 (fixed)	0.045 (fixed)	0.061 (fixed)	0.013 (fixed)
v_{los} (10^3 km s^{-1})	$-1.086^{+0.074}_{-0.078}$	$-1.046^{+0.082}_{-0.082}$	$-1.241^{+0.078}_{-0.070}$	$-1.155^{+0.062}_{-0.064}$	$-0.622^{+0.079}_{-0.082}$
σ_{los} (km s^{-1})	$713.4^{+96.5}_{-84.5}$	$679.7^{+120.7}_{-106.1}$	$579.8^{+93.0}_{-86.4}$	$419.6^{+123.9}_{-134.9}$	$566.6^{+103.7}_{-103.1}$
Norm. ($10^{-14}/4\pi$ cm^{-5})	$0.134^{+0.007}_{-0.007}$	$0.206^{+0.012}_{-0.012}$	$0.253^{+0.013}_{-0.015}$	$0.208^{+0.008}_{-0.007}$	$0.115^{+0.006}_{-0.008}$
N_H (10^{22} cm^{-2})	0.585 (fixed)	0.590 (fixed)	0.626 (fixed)	0.696 (fixed)	0.594 (fixed)
C-statistics (dof)	1043.63 (979)	1100.92 (978)	1155.67 (981)	1259.09 (976)	1183.64 (975)

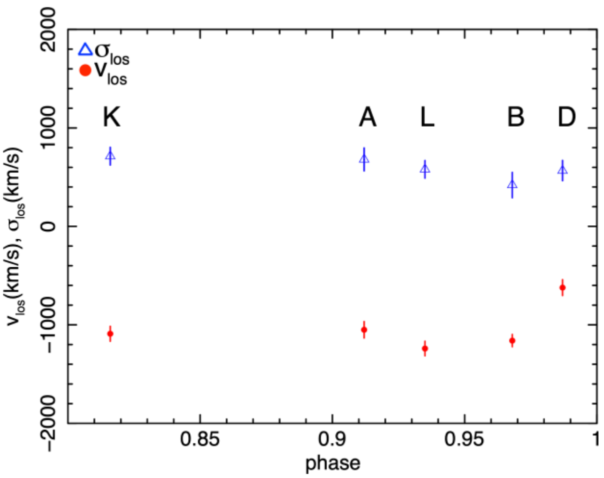

Figure 5. The line-of-sight velocity (v_{los}) and velocity dispersion (σ_{los}) of Ne (summarized in Table 5) plotted as a function of orbital phase. At all phases, the line-of-sight velocity of Ne is blue-shifted. The maximum blue shift and velocity dispersion are about 1200 km s^{-1} and about 700 km s^{-1}, respectively.

(see Section 4.1.4). Accordingly, the location of the shock front can be obtained by calculating the balance of the ram pressure between the stellar winds. The ram pressure $P(r)$ is expressed by the following equation using the mass density of the stellar wind ρ, its velocity v, the terminal velocity v_∞, the radius of the star R_*, and the mass ejection rate $\dot{M}$.

$$P(r) = \rho(r)v(r)^2 = \frac{\dot{M}}{4\pi r^2}v(r) = \frac{\dot{M}v_\infty}{4\pi r^2}\left(1-\frac{R_*}{r}\right). \quad (2)$$

Note here that we assume $\beta = 1$ wind velocity law for both stars (Section 1). This does not raise, however, any practical problem, since, for reasonable values of β, the stagnation point is formed at a place whose distance is much larger than the radius of the WR star ($r >> R_{wr}$), and the wind pressure is not different between the cases $\beta = 1$ and $\beta >> 1$ (fig. 14 of Sugawara et al. 2015).

The ram pressure balance between the two stellar wind components is as follows (Usov 1992; Cantó, Raga & Wilkin 1996; Pittard & Stevens 1997):

$$\rho_{wr}(r_{wr})\, v_{wr}^2(r_{wr}) = \rho_o(r_o)\, v_o^2(r_o), \quad (3)$$

where r_{wr} and v_o represent the distance from the WR star and the O star to the stagnation point, respectively, and $r_{wr} + r_o = d$ (distance between the two stars, see Fig. 7). Now we introduce the parameter φ, defined by the ratio of the momentum rates of the two stellar winds, with the following equation.

$$\sqrt{\frac{\dot{M}_o v_{\infty,o}}{\dot{M}_{wr} v_{\infty,wr}}} \equiv \varphi. \quad (4)$$

Then, by eliminating r_o by using d and by normalizing the whole expression by d, we get the following equation:

$$\left(\frac{1-\frac{r_{wr}}{d}}{\frac{r_{wr}}{d}}\right)^3 \frac{\frac{r_{wr}}{d}-\frac{R_{wr}}{d}}{1-\frac{r_{wr}}{d}-\frac{R_o}{d}} = \varphi^2. \quad (5)$$

Since $R_o/d = 0.076$ at periastron passage, R_{wr}/d (= 1/13 of R_o/d at the same phase) << 1, we neglect these two terms in equation (5). As a result, we obtain the distance of the stagnation point from the WR star as

$$r_{wr} = \frac{1}{1+\varphi}d. \quad (6)$$

4.1.3 Geometry of the shock cone

Placing the stagnation point obtained above at the origin as shown in Fig. 7, we calculate the cone of the subsequent shock front by taking into account the pressure balance of the stellar winds normal to the cone. We write the unit vectors of the normal direction at the point (x, y) on the shock cone as $\boldsymbol{n}_{wr}$ and $\boldsymbol{n}_o$ ($= -\boldsymbol{n}_{wr}$), respectively, and then the balance of the ram pressure in the direction perpendicular to the shock front is

$$\boldsymbol{P}_{wr}(r_{wr}) \cdot \boldsymbol{n}_{wr} = \boldsymbol{P}_o(r_o) \cdot \boldsymbol{n}_o. \quad (7)$$

By solving equation (7), we finally obtain the following:

$$\frac{d\xi}{d\eta} = \frac{1}{\eta}\left\{\xi + \frac{\frac{1}{\lambda_{wr}^3}\left(1-\frac{\Lambda_{wr}}{\lambda_{wr}}\right) - \frac{\varphi^3}{\lambda_o^3}\left(1-\frac{\Lambda_o}{\lambda_o}\right)}{\frac{1}{\lambda_{wr}^3}\left(1-\frac{\Lambda_{wr}}{\lambda_{wr}}\right) + \frac{\varphi^2}{\lambda_o^3}\left(1-\frac{\Lambda_o}{\lambda_o}\right)}\,\frac{1}{1+\varphi}\right\}, \quad (8)$$

where x and y in Fig. 7, distances of the two stars from the stagnation point r_{wr} and r_o, and the radii of the two stars R_{wr},

Table 6. Best-fitting parameters of the He-like triplet of Ne using the model comprised of bvapec and three zgauss components, which represent a resonance line, intercombination lines, and a forbidden line. The Ne abundance is fixed at zero, and the other parameters of bvapec and tbabs are fixed at the best-fitting values obtained from the fitting including the H-like Ne line (Table 5). The line-of-sight velocity $v_{\rm los}$ is not constrained very well solely with the He-like line. Hence the fitting is performed with $v_{\rm los}$ at its best-fitting value, and at the minimum and maximum values separately, that are obtained from the fit including the H-like Ne line as well (Table 5). $E_{\rm f}$, $E_{\rm i}$, and $E_{\rm r}$ are fixed at the rest-frame energies of the He-like triplet of Ne, and they are effectively floated with the common value of the line-of-sight velocity ($v_{\rm los}$). $\sigma_{\rm f}$ is variable. $\sigma_{\rm i}$ and $\sigma_{\rm r}$ are linked to $\sigma_{\rm f}$ with their line energy ratios ($E_{\rm i}/E_{\rm f}$ and $E_{\rm r}/E_{\rm f}$, respectively). Consequently, the free parameters of the fitting are $\sigma_{\rm f}$ and Norm.$_{\rm f}$, Norm.$_{\rm i}$, and Norm.$_{\rm r}$ which are intensities of the lines.

ID		K			A			L			B			D	
Phase		0.816			0.912			0.935			0.968			0.987	
	min	Best fit	max	min	Best fit	max	min	Best fit	max	min	Best fit	max	min	best-fit	max
$v_{\rm los}$ (10^3 km s^{-1}) (fixed)	−1.164	−1.086	−1.011	−1.128	−1.046	−0.963	−1.310	−1.241	−1.163	−1.219	−1.155	−1.092	−0.704	−0.622	−0.543
kT (keV)		0.453 (fixed)			0.474 (fixed)			0.469 (fixed)			0.839 (fixed)			0.584 (fixed)	
$Z_{\rm Ne}$		0 (fixed)			0 (fixed)			0 (fixed)			0 (fixed)			0 (fixed)	
σ_v (km s^{-1})		713.4 (fixed)			679.7 (fixed)			579.8 (fixed)			417.9 (fixed)			566.6 (fixed)	
Norm. ($10^{-14}/4\pi$ cm^{-5})		0.145 (fixed)			0.206 (fixed)			0.253 (fixed)			0.208 (fixed)			0.115 (fixed)	
$N_{\rm H}$ (10^{22} cm^{-2})		0.585 (fixed)			0.590 (fixed)			0.626 (fixed)			0.696 (fixed)			0.594 (fixed)	
$E_{\rm f}$ (keV)		0.905 (fixed)			0.905 (fixed)			0.905 (fixed)			0.905 (fixed)			0.905 (fixed)	
$\sigma_{\rm f}$ (10^{-3} keV)	$2.505^{+0.465}_{-0.420}$	$2.586^{+0.462}_{-0.419}$	$2.665^{+0.401}_{-0.433}$	$1.945^{+0.728}_{-0.475}$	$2.071^{+0.727}_{-0.450}$	$2.218^{+0.701}_{-0.452}$	$1.949^{+0.610}_{-0.458}$	$2.036^{+0.633}_{-0.445}$	$2.162^{+0.636}_{-0.471}$	$0.664^{+0.799}_{-0.388}$	$0.654^{+0.694}_{-0.436}$	$0.687^{+0.701}_{-0.676}$	$1.975^{+0.793}_{-0.510}$	$1.999^{+0.805}_{-0.576}$	$2.091^{+0.747}_{-0.598}$
Norm.$_{\rm f}$ (10^{-5} s^{-1} cm^{-2})	$8.794^{+1.615}_{-1.557}$	$8.802^{+1.533}_{-1.559}$	$8.792^{+1.523}_{-1.585}$	$9.611^{+2.420}_{-2.064}$	$9.471^{+2.417}_{-2.103}$	$9.316^{+2.339}_{-2.032}$	$11.767^{+2.488}_{-2.126}$	$11.831^{+2.544}_{-2.248}$	$11.895^{+2.482}_{-2.373}$	$7.721^{+1.990}_{-1.809}$	$7.693^{+2.004}_{-1.870}$	$7.607^{+1.995}_{-1.960}$	$3.867^{+1.099}_{-1.102}$	$3.768^{+1.106}_{-1.062}$	$3.684^{+1.135}_{-1.030}$
$E_{\rm i}$ (keV)		0.915 (fixed)			0.915 (fixed)			0.915 (fixed)			0.915 (fixed)			0.915 (fixed)	
Norm.$_{\rm i}$ (10^{-5} s^{-1} cm^{-2})	$2.134^{+1.898}_{-1.638}$	$1.638^{+1.997}_{-1.377}$	$1.206^{+2.048}_{-1.019}$	$6.185^{+2.572}_{-2.757}$	$5.783^{+2.619}_{-2.669}$	$5.383^{+2.806}_{-2.788}$	$4.639^{+2.447}_{-2.737}$	$4.186^{+2.560}_{-2.630}$	$3.652^{+2.671}_{-2.553}$	$1.208^{+2.321}_{-0.978}$	$1.169^{+2.244}_{-0.958}$	$1.185^{+2.159}_{-1.015}$	$1.970^{+1.274}_{-1.201}$	$1.750^{+1.308}_{-1.168}$	$1.526^{+1.282}_{-1.152}$
$E_{\rm r}$ (keV)		0.922 (fixed)			0.922 (fixed)			0.922 (fixed)			0.922 (fixed)			0.922 (fixed)	
Norm.$_{\rm r}$ (10^{-5} s^{-1} cm^{-2})	$19.814^{+2.345}_{-2.246}$	$20.342^{+2.302}_{-2.266}$	$20.805^{+2.080}_{-2.344}$	$20.561^{+3.149}_{-2.673}$	$21.149^{+3.381}_{-2.688}$	$21.741^{+3.234}_{-3.000}$	$20.343^{+3.300}_{-2.787}$	$20.879^{+3.262}_{-2.900}$	$21.507^{+3.279}_{-2.829}$	$8.820^{+1.965}_{-2.293}$	$8.917^{+2.145}_{-2.259}$	$8.932^{+2.279}_{-2.146}$	$6.320^{+1.576}_{-1.330}$	$6.598^{+1.489}_{-1.357}$	$6.876^{+1.516}_{-1.390}$
C-statistics (dof)		527.46 (522)			591.58 (523)			591.74 (525)			665.94 (519)			630.80 (520)	

$R_{\rm o}$ are normalized with the distance between the two stars d as follows:

$$\xi \equiv \frac{x}{d}, \eta \equiv \frac{y}{d}, \lambda_{\rm wr} \equiv \frac{r_{\rm wr}}{d}, \lambda_{\rm o} \equiv \frac{r_{\rm o}}{d},$$

$$\Lambda_{\rm wr} \equiv \frac{R_{\rm wr}}{d}, \Lambda_{\rm o} \equiv \frac{R_{\rm o}}{d}. \tag{9}$$

$$\lambda_{\rm wr} = \frac{r_{\rm wr}}{d} = \sqrt{\left(\xi + \frac{1}{1+\varphi}\right)^2 + \eta^2}. \tag{10}$$

$$\lambda_{\rm o} = \frac{r_{\rm o}}{d} = \sqrt{\left(\xi - \frac{\varphi}{1+\varphi}\right)^2 + \eta^2}. \tag{11}$$

Detailed algebra to derive equation (8) is summarized in appendix A. By solving equation (8) numerically, we obtain the shape of the shock cone, which is shown in Fig. 8. It is found that the shape of the normalized shock cone is nearly the same for all phases, although the outward opening angle of the shock cone becomes slightly smaller as the separation d decreases. This is because the wind collision occurs before the wind velocity of the O star reaches terminal velocity.

4.1.4 *Line-of-sight velocity and its dispersion*

Now that we have the shape of the shock cone, we next calculate the ratio of the radial velocity and the velocity dispersion along the shock cone. When the O star is on the x-axis like in Fig. 1, the velocity vector of the plasma $\boldsymbol{t}$, flowing along the shock cone, can be written as follows with the angle around the x-axis ψ.

$$\boldsymbol{t}(x, y, \psi) = \begin{pmatrix} \Delta x \\ \Delta y \cos\psi \\ \Delta y \sin\psi \end{pmatrix}. \tag{12}$$

In what follows, we neglect the effect of Coriolis forces which is expected to be small at phases before the periastron passage[4] and we assume that the shock front is axisymmetric with respect to the line connecting the two stars because the orbital speed of the O star is negligibly small compared with the wind speed at the phases we analyse in this paper. At the phases other than periastron, we can rotate this vector by $-\theta$, the true anomaly, around the z-axis. Writing that transformation as $R_z(-\theta)$, we obtain the resultant vector as follows:

$$\begin{aligned} \boldsymbol{t}(x, y, \psi, \theta) = &\ R_z(-\theta)\, \boldsymbol{t}(x, y, \psi) \\ = &\begin{pmatrix} \cos\theta & \sin\theta & 0 \\ -\sin\theta & \cos\theta & 0 \\ 0 & 0 & 1 \end{pmatrix} \begin{pmatrix} \Delta x \\ \Delta y \cos\psi \\ \Delta y \sin\psi \end{pmatrix} \\ = &\begin{pmatrix} \Delta x \cos\theta + \Delta y \cos\psi \sin\theta \\ -\Delta x \sin\theta + \Delta y \cos\psi \cos\theta \\ \Delta y \sin\psi \end{pmatrix}. \end{aligned} \tag{13}$$

In order to convert this vector into the configuration viewed from the observer, we rotate it by $-\omega$ around the z-axis, $-i$ around the x-axis, and $-\Omega$ around the z-axis in this order. Note that, prior to these rotations, the z-axis is perpendicular to the plane of this paper, and points to the reader (namely Fig. 1). We write this rotation as $R_{z\text{-}x\text{-}z}(-\Omega, -i, -\omega)$. Then, the vector on the celestial sphere is $R_{z\text{-}x\text{-}z}(-\Omega, -i, -\omega)\boldsymbol{t}(x, y, \psi, \theta)$ (see Table 1 for the values of ω, i, and Ω). Note also that by applying this rotation to the orbit shown in Fig. 1, we obtain the real orbit of WR140 projected on

[4] http://harmas.arc.hokkai-s-u.ac.jp/okazaki/cwb/WR140/index.html

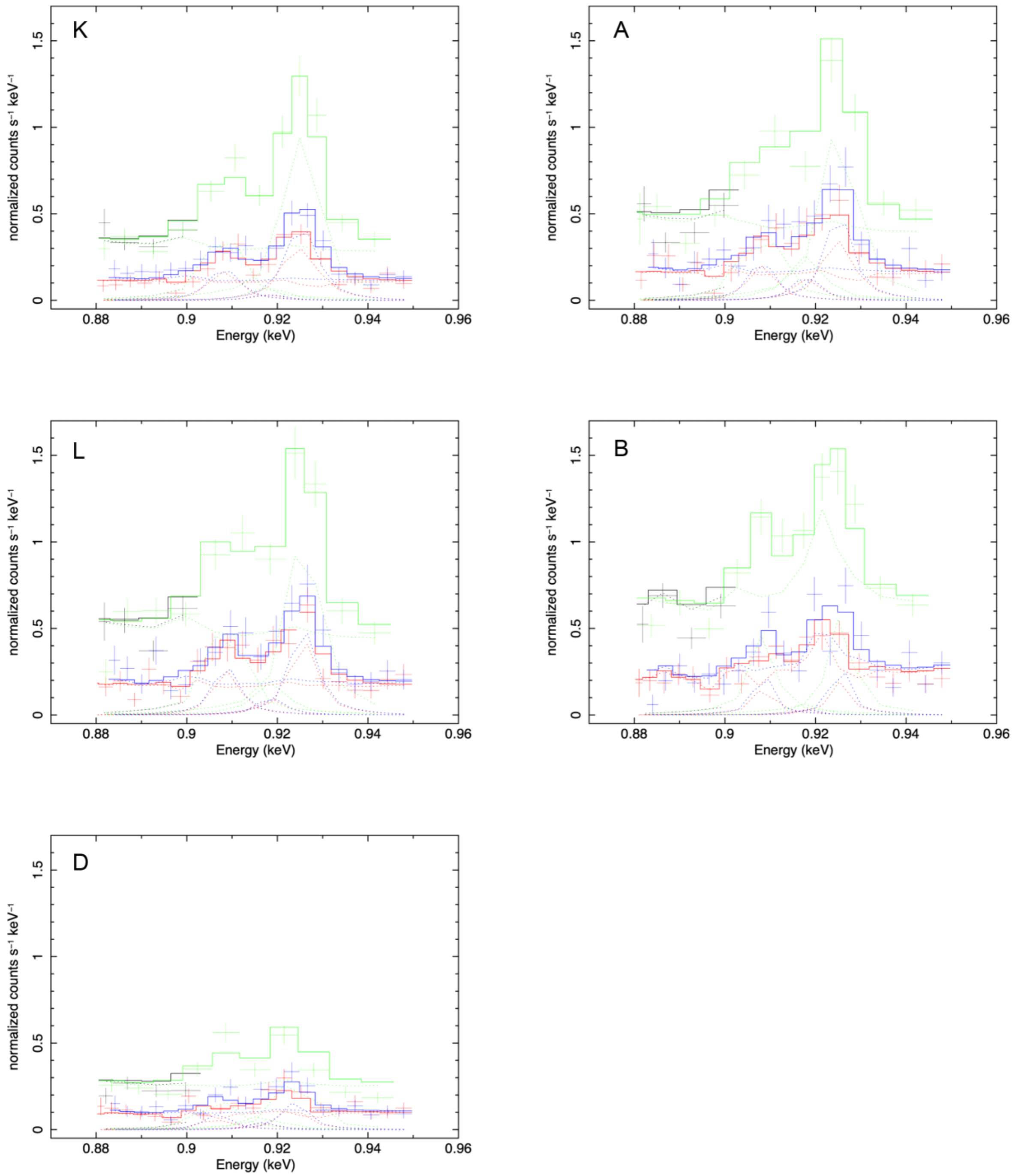

Figure 6. The spectra at phases K (0.816), A (0.912), L (0.935), B (0.968), and D (0.987) in the band 0.88–0.95 keV that entirely covers the Kα lines of Ne IX. The colour assignment of the data and the model are the same as those in Fig. 3. The model is bvapec with Ne abundance being set equal to zero plus three zgauss lines that represent the resonance, intercombination, and forbidden lines. This entire emission model is attenuated with photoelectric absorption represented by the model tabs. The best-fitting parameters of this fit are summarized in Table 6.

to the celestial sphere, as shown in Monnier et al. (2011). In this framework, before the rotations, the x-axis of Fig. 1 points to the celestial north pole. Since the direction of the line of sight before the rotations is $+z$, the radial velocity $v_{\rm los}$ is the z component of this vector, and can be written as follows:

$$\begin{aligned} v_{\rm los}(x, y, \psi, \theta, \Omega, i, \omega) &= [R_{z\text{-}x\text{-}z}(-\Omega, -i, -\omega)\boldsymbol{t}(x, y, \psi, \theta)]_z \\ &= \Delta x \sin i \sin(\theta+\omega) \\ &\quad +\Delta y \left[\sin i \cos\psi \cos(\theta+\omega) \right. \\ &\quad \left. + \sin\psi \cos i \right]. \end{aligned} \tag{14}$$

We take an average over the angle ψ,

$$\langle v_{\rm los}\rangle = \Delta x \sin i \sin(\theta+\omega). \tag{15}$$

This equation should be compared with the observed $v_{\rm los}$ profile plotted in Fig. 5. If we assume $i = 0$ in this equation, the radial velocity is 0. Of course this is because we would then be looking at WR140 from the direction perpendicular to the orbital plane. It is also found that the radial velocity does not depend on the rotation $-\Omega$ around the z-axis. This is because the line of sight is along the z-axis. At phases K (0.816), A (0.912), L (0.935), B (0.968), and D

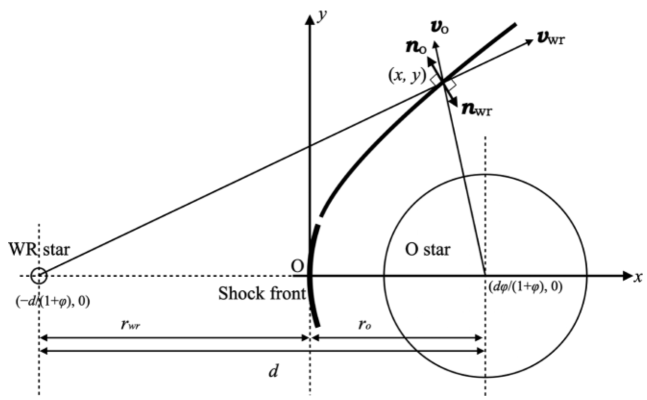

Figure 7. Scheme of the WR140 binary for the calculation of the shape of the shock cone. The location of the head-on collision (stagnation point) is placed at the origin. $\boldsymbol{v}_{\rm wr}$ and $\boldsymbol{v}_{\rm o}$ are the velocity vectors of the stellar winds from the WR star and the O star, respectively. We write the unit vectors perpendicular to the shock cone at the point (x, y) as $\boldsymbol{n}_{\rm wr}$ and $\boldsymbol{n}_{\rm o}$ $(= -\boldsymbol{n}_{\rm wr})$.

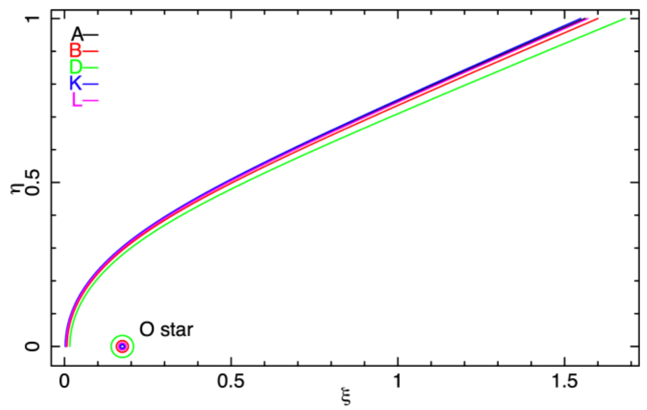

Figure 8. The shape of the shock cone at the phases K (0.816), A (0.912), L (0.935), B (0.968), and D (0.987). The vertical and horizontal axes y and x in Fig. 7 are normalized by the separation of the two component stars d (equation 9) and labelled η and ξ, respectively. The size of the O stars are also scaled accordingly. The normalized shock cone is nearly the same for all phases.

(0.987), when WR140 is clearly detected with the RGS, θ is in the range 198°-259° (Table 3). Since $\omega = 46\fdg8$ (see Table 1), $\theta + \omega$ is in the range 245°–306°, and hence $\langle v_{\rm los}\rangle < 0$ from equation (15). This agrees with the observed facts (Table 5, Fig. 5).

On the other hand, the velocity dispersion $\sigma_{\rm los}(x, y, \theta, \Omega, i, \omega)$ can be written as follows:

$$\sigma_{\rm los}^2(x, y, \theta, \Omega, i, \omega) = \left\langle (v_{\rm los}(x, y, \psi, \theta, \Omega, i, \omega) - \langle v_{\rm los}(x, y, \theta, \Omega, i, \omega)\rangle)^2 \right\rangle . \quad (16)$$

Using equations (14) and (15), taking an average over ψ, it can be written as

$$\sigma_{\rm los}^2 = \frac{1}{2}(\Delta y)^2[\sin^2 i \cos^2(\theta+\omega) + \cos^2 i]. \quad (17)$$

We then obtain the ratio of the line-of-sight velocity and its dispersion $v_{\rm los}/\sigma_{\rm los}$ as follows:

$$\frac{v_{\rm los}}{\sigma_{\rm los}} = \frac{\Delta x}{\Delta y}\frac{\sqrt{2}\sin i\ \sin(\theta+\omega)}{\sqrt{\sin^2 i\ \cos^2(\theta+\omega)+\cos^2 i}}. \quad (18)$$

This should be compared with the ratio of the radial velocity and the velocity dispersion of the observed data (Table 5, Fig. 5).

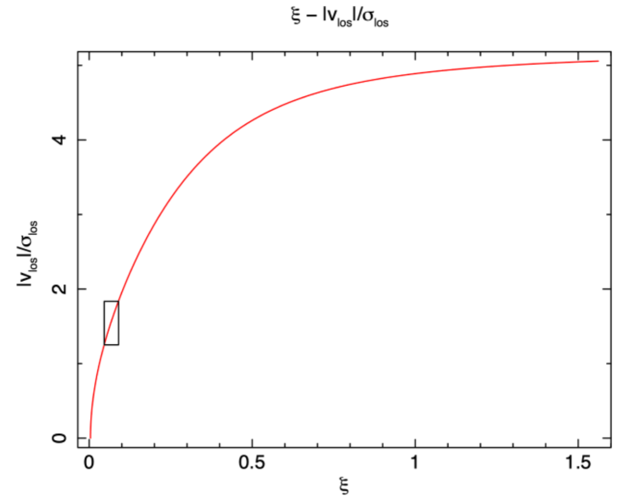

Figure 9. The curve of $|v_{\rm los}|/\sigma_{\rm los}$ as a function of ξ at the orbital phase A (0.912). Since $|v_{\rm los}|$ increases whereas $\sigma_{\rm los}$ decreases both monotonically as the distance from the stagnation point increases, $|v_{\rm los}|/\sigma_{\rm los}$ increase monotonically. The vertical side of the black box corresponds to the allowed range of the observed $|v_{\rm los}|/\sigma_{\rm los}$. We can estimate the value of ξ at the Ne line-emission site from the two intersectional points between the box and the curve of $|v_{\rm los}|/\sigma_{\rm los}$.

From equation (17), when we take $i = \pi/2$ and $\theta + \omega = \pi/2$ or $3\pi/2$, the velocity dispersion is 0. In that case, the observer would then be in the orbital plane and the two stars in the configuration of the conjunction with each other. At that time, the Ne emission site on the shock cone would be symmetric around the line of sight to the observer. At the same time, $|v_{\rm los}|$ would have its the maximum value. In Fig. 5, on the other hand, the observed $\sigma_{\rm los}$ and $|v_{\rm los}|$ take their minimum and maximum value, respectively, between phases B (0.968) and L (0.935), close to the O star's inferior conjunction. This agreement between the calculations in equations (15)–(17) and the measurements in Fig. 5 strongly suggests that our assumption that the shocked plasma flows along the shock cone rather like a laminar flow is correct to a first order approximation, and the effect of turbulence is probably rather minor at the Ne line-emission site.

At phase A (0.912), the curve of the ratio $|v_{\rm los}|/\sigma_{\rm los}$ as a function of ξ is shown in Fig. 9. We plot the minimum and maximum values of the ratio of the observed data on this curve, and estimate the value of ξ at the Ne line-emission site from the intersection points. The same operation is performed for phase B (0.968), D (0.987), K (0.816), and L (0.935), and the location of each Ne emission site is plotted on the shock cone in Fig. 10. In addition, we obtain the distance from the stagnation point by multiplying the distance d between the two stars of each phase to ξ and η in Table 7. For all phases, we find that the Ne line-emission site is located at a distance of $(0.9\text{–}8.9) \times 10^{13}$ cm from the stagnation point. The distances from the O star are utilized to evaluate the photoexcitation effect on the electron density evaluation in Section 4.2.2.

4.2 Plasma density of Ne line-emission site

4.2.1 Density diagnosis

In the previous section, we obtained the location of the Ne line-emission site at each phase on the shock cone. We will next calculate the plasma electron density from intensity ratios of the He-like

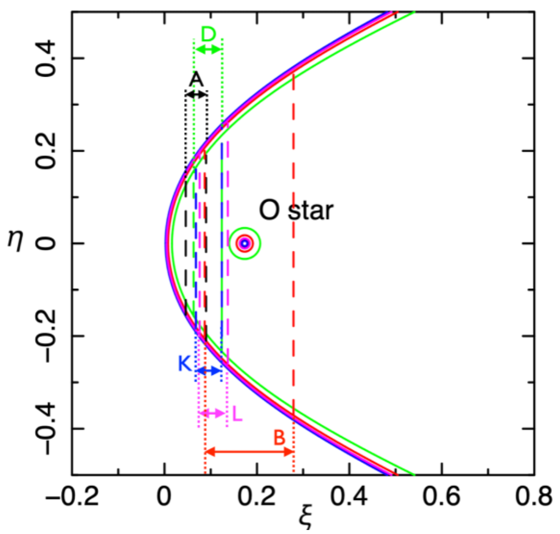

Figure 10. The location of the Ne line-emission site at each phase on the shock cone. The vertical and horizontal axes *y* and *x* in Fig. 7 are normalized by the distance between the two components stars *d* and labelled as η and ξ, respectively. The size of the O star is also normalized for each phase. The normalized emission site is nearly the same for all phases.

triplet components, using SPEX version 3.06.01,[5] a plasma code developed by SRON.[6] In general, as described in Section 3.4, the initial state of the forbidden line ($^3S_1$) of the He-like triplet has a relatively long lifetime, and it can be excited to the initial state of the intercombination lines ($^3P_{1,2}$) by an electron impact before direct de-excitation occurs. Thus, it is expected that the intensity of the intercombination lines increases and that of the forbidden line decreases by the same amount as the plasma density increases.

In order to evaluate the electron density from the Ne Kα lines, we calculate theoretical intensities of the forbidden, intercombination, and resonance lines as a function of the electron number density using CIE,[7] a model of the spectrum of the plasma in collisional ionization equilibrium. Sugawara et al. (2015) successfully fitted the model vpshock to the *Suzaku* XIS spectra in the band above 2 keV, which represents an X-ray spectrum from a constant temperature plane-paralell shock plasma.[8] This model can handle a plasma at ionizing phase. Their fits, however, resulted in the ionization parameter $\tau_u = n_e t$ = 4–8 $\times$ 10^{12} cm^{-3} s^{-1}, where *t* is the lapse time since the plasma experiences the shock. This large τ_u indicates that the plasma is already in ionization equilibrium ($\log n_e t \gtrsim 12$ in cgs unit, Masai 1984). Thus we have adopted the CIE model here. The CIE model allows us to set an electron temperature and an electron density as parameters. Of these parameters, we input the electron temperature obtained from the fits of the H-like and He-like lines from Ne [0.474 keV at phase A (0.912); see Table 5] into the model. Next, we vary the electron number density n_e and get the intensities of the triplet components and calculate the curves of the ratios *f*/*r* and *i*/*r* as a function of n_e (red and blue lines in Fig. 11, respectively). On these curves, we plot the values of *f*/*r* and *i*/*r* with their error obtained (Table 6), and estimate the electron number density from the intersection of the error boxes with the curves. We take the overlapping region of the allowed density ranges from *f*/*r* and *i*/*r*, as indicated by the black arrows in Fig. 11. As a result, the electron number density from the Ne IX lines at phase A (0.912) is in the range $0.31 \times 10^{12} < n_e < 1.76 \times 10^{12}$ cm^{-3}.

We do the same analysis for the other four phases (Fig. 12). Table 8 shows the electron number density at phases K (0.816), A (0.912), L (0.935), B (0.968), and D (0.987) thus measured. At phase K (0.816), the allowed ranges of the density from the ratios *f*/*r* and *i*/*r* do not overlap. This is probably because the energy resolution of the RGS is not high enough to resolve the weak and somewhat broad intercombination lines (*i*) from the resonance line (*r*). We therefore adopt the density obtained only with *f*/*r* at phase K (0.816), 0.47−2.83$\times$ 10^{12} cm^{-3}. Except for phases K (0.816) and A (0.912), only an upper limit is obtained at the other phases.

Pollock et al. (2005) found that the *f*/*i* ratio is >4.0, at the pre-periastron phase 0.986 (according to the ephemeris we adopt) with the *Chandra* HETG which is larger than the theoretical value of the low density limit 3.4. Our result at phase D (0.987) is, on the other hand, 2.2 $\pm$ 1.6, consistent to the theoretical low density limit. They also pointed out that some lines from Fe XIX contaminate the intercombination line of Ne at phase 0.986, which is close to our phase D (0.987). In our spectral fit at phase K (0.816) and A (0.912) where we obtain finite values of the electron number density, however, we found no such contamination. This can at least partly be ascribed to the fact that the abundance of Fe is as small as 0.04 solar. An Fe line appears if we artificially increase the Fe abundance.

We note that the intensity ratio that is sensitive to the density is *f*/*i*. Practically, however, this ratio is not constrained well if either *f* or *i* are weak. In addition, the intensity $i + f$ is constant from their nature and its ratio to *r* is uniquely determined at a given temperature. We were not able to reflect these two constraints in the fitting procedure in XSPEC. We can overcome all these difficulties technically by using *f*/*r* and *i*/*r* in the way described above.

One may suspect that the electron number density should be much higher at orbital phases closer to the periastron [at phase D (0.987) rather than K (0.816) and A (0.912)], because the two-component stars are closer and hence the plasma at the stagnation point should have higher density. From Fig. 10, the Ne line-emission site overlaps among all orbital phases in the non-dimensional ξ-η plane. This implies that the Ne line-emission site at orbital phases K (0.816) and A (0.912) is further away in the real *x*–*y* plane from the stagnation point. This may mean that it takes some time for the clumping of the plasma to develop itself. Also it may be possible that the plasma is adiabatically cooled down to a temperature that is too low to emit the Ne lines at later orbital phases, before the clumping develops. This is, however, only speculation at this moment. To understand the fact that the density seems higher at the earlier phases K (0.816) and A (0.912), we need to obtain the temperature and density profiles of the plasma along the shock cone. This can be done by next generation observatories which are equipped with high-resolution spectrometers that have larger effective area than the *Chandra* HETG and the *XMM–Newton* RGS. As a matter of fact, Pollock et al. (2005) found He-like triplets from O to Fe with the *Chandra* HETG, which are useful for such diagnosis.

As shown above, we can evaluate the temperature and the density of the part of the plasma emitting the Ne emission lines with the intensity ratio of the He-like and H-like Kα lines, and the ratios *f*/*r* and *i*/*r* of the He-like triplet, respectively. In addition, from the ratio $|v_{\rm los}|/\sigma_{\rm los}$, we can identify the mean location of the Ne line-emission site. By doing the same thing with other elements, we can deduce

[5] https://www.sron.nl/astrophysics-spex

[6] https://www.sron.nl

[7] https://var.sron.nl/SPEX-doc/manualv3.05/manualse49.html

[8] https://heasarc.gsfc.nasa.gov/xanadu/xspec/manual/node217.html

Table 7. The Ne line-emission site for all phases.

Phase	ξ	η	x (10^{13} cm)	y (10^{13} cm)	Real distance (10^{13} cm) From the WR star	From the O star	From the stagnation point
K (0.816)	0.068–0.124	0.192–0.258	2.1–3.8	6.0–8.0	28.4–30.6	6.8–8.2	6.3–8.9
A (0.912)	0.046–0.090	0.154–0.218	0.9–1.8	3.1–4.4	17.9–19.1	4.0–4.7	3.3–4.8
L (0.935)	0.076–0.137	0.199–0.266	1.3–2.3	3.3–4.4	15.4–16.7	3.7–4.5	3.5–5.0
B (0.968)	0.087–0.279	0.206–0.371	0.9–2.9	2.1–3.8	9.6–12.0	2.3–4.0	2.3–4.8
D (0.987)	0.063–0.124	0.159–0.234	0.3–0.7	0.9–1.3	4.9–5.3	1.0–1.3	0.9–1.4

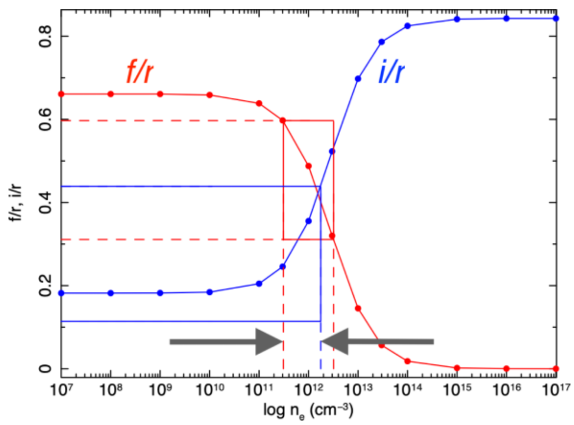

Figure 11. Density diagnostic of the plasma with the intensity ratio of the He-like triplet of Ne at orbital phase A (0.912). The red and blue curves represent the relations of the line intensity ratio (*f*/*r*, *i*/*r*) versus the electron number density at phase A (0.912) temperature 0.474 keV (Table 5). The vertical side of the boxes indicates the range of the intensity ratio allowed from the observation and the horizontal side of the boxes is the resultant electron number density.

the profile of the temperature and the density of the plasma along the shock cone.

4.2.2 *Comparison with the local wind densities*

Table 9 shows the local electron number densities of the WR star wind $n_{\rm e,\,wr}$ and the O star wind $n_{\rm e,\,o}$, were it not for the shock at the Ne line-emission site for all phases. They are obtained simply according to equations (1) and (2), with the real distances from the WR star and from the O star (Table 7). Here, we assume that the WR wind is composed mainly of He.

From Table 9, we find that the observed plasma electron densities (Table 8) are much greater than those of the stellar wind $n_{\rm e,\,wr}$ and $n_{\rm e,\,o}$ at the Ne emission site by 6 orders of magnitude. The intensities of the He-like triplet of Ne summarized in Table 6 and their ratios are, of course, robust, because they are observed quantities. It is, however, not easy to realize such high density.

Let us first assume that the shocked plasma flow is uniform (not clumpy) and try to estimate the electron number density at the Ne line-emission site at phase A (0.912). Taking the pre-shock velocity $v_1 = v_{\infty,\,\rm wr}$ and assuming the temperature of the pre-shock flow T_1 to be 1×10^4 K, being composed only of fully ionized He and associated electrons, we obtain the Mach number of the pre-shock flow $M_1 = v_1/c_1 \simeq 280$. Although such a highly supersonic flow can enhance the density by only a factor of 4 at the stagnation point through a strong shock, the enhancement factor of the temperature there is as large as $2\gamma(\gamma-1)M_1^2/(\gamma+1)^2 \simeq 4.1\times10^4$ as per the Rankine–Hugoniot relations. This enhancement factor can be applied to the density if the plasma experiences highly strong radiative cooling and goes back to the original temperature 1×10^4 K, according to the equation of state $\rho T \propto P$, which is constant as long as the post-shock plasma flow is isobaric. In that case, the density can be as high as $\simeq 10^{11}$ cm^{-3}, with the phase A density $n_{\rm e,\,wr}$ in Table 9. The Ne line-emission site is, however, located somewhat downstream from the stagnation point, and the density is probably reduced from this number. What is worse, the temperature there at phase A (0.912) is 0.474 keV ($= 5.50\times10^6$ K). Such a warm flow can produce an electron number density as low as $\simeq 4\times10^8$ cm^{-3}.

We remark, however, that the plasma at the Ne line-emission site is not formed locally but the result of the integration of the whole plasma flow from the stagnation point, which can help enhance the density at the Ne line-emission site. The other possibility to explain the high density is plasma instabilities (Sugawara et al. 2015). As pointed out by Pittard (2007), density clumps that probably exist in the pre-shock stellar wind are rapidly destroyed after entering the colliding shock. New clumps, however, can develop themselves after the shock, owing to a few mechanisms of instability, such as the Kelvin–Helmholtz instability (section 2.4 of Stevens, Blondin & Pollock 1992). Such instabilities are expected to help the density enhancement in the post-shock plasma flow.

4.2.3 *Photoexcitation correction to the density evaluation*

The densities in Table 8 are obtained by assuming only collisional excitation. As mentioned in Section 4.1.1, we need to correct for the photoexcitation due to extreme UV radiation of the O star, the prime UV source, for the WR star is much further away from the Ne line-emission site. Now that we identify the Ne line-emission site, we calculate the effect of photoexcitation at all phases, using the distance of the emission site from the O star. In general, we can write the rate coefficient of excitation from the initial state i to the final state j by an electron impact as

$$q_{ij}(T_{\rm e}) = \frac{8.63\times10^{-6}}{\omega_i T_{\rm e}^{1/2}} e^{-E_{ij}/kT_{\rm e}} \gamma_{ij}(T_{\rm e}) \qquad [{\rm cm^{-3}\ s^{-1}}], \tag{19}$$

(Pradhan, Norcross & Hummer 1981), where the states i and j now correspond to the upper levels of the forbidden and intercombination lines, which are $^3{\rm S}_1$ and $^3{\rm P}_{2,\,1}$, respectively, ω_i is the degeneracy factor of the initial state $^3{\rm S}_1$, $T_{\rm e}$ is the electron temperature, where we adopt the $kT_{\rm e}$ values listed in Table 5, γ_{ij} is the Maxwellian-averaged collision strength, and E_{ij} is the energy difference between the levels. Multiplying this by the electron density of the plasma $n_{\rm e}$, we can obtain the collisional excitation rate from $^3{\rm S}_1$ to $^3{\rm P}_{2,\,1}$ per volume. In reality, however, as described in Section 4.1.1, we need to take into account the effect of photoexcitation by extreme ultraviolet photons from the O star, the effect of which can be written as

$$\Gamma_{ij}(T_{\rm r}, \nu_{ij}) = \frac{\pi e^2}{m_{\rm e}c} f_{ij}\, W \frac{\pi B(T_{\rm r}, \nu_{ij})}{h\nu_{ij}} \qquad [{\rm s^{-1}}], \tag{20}$$

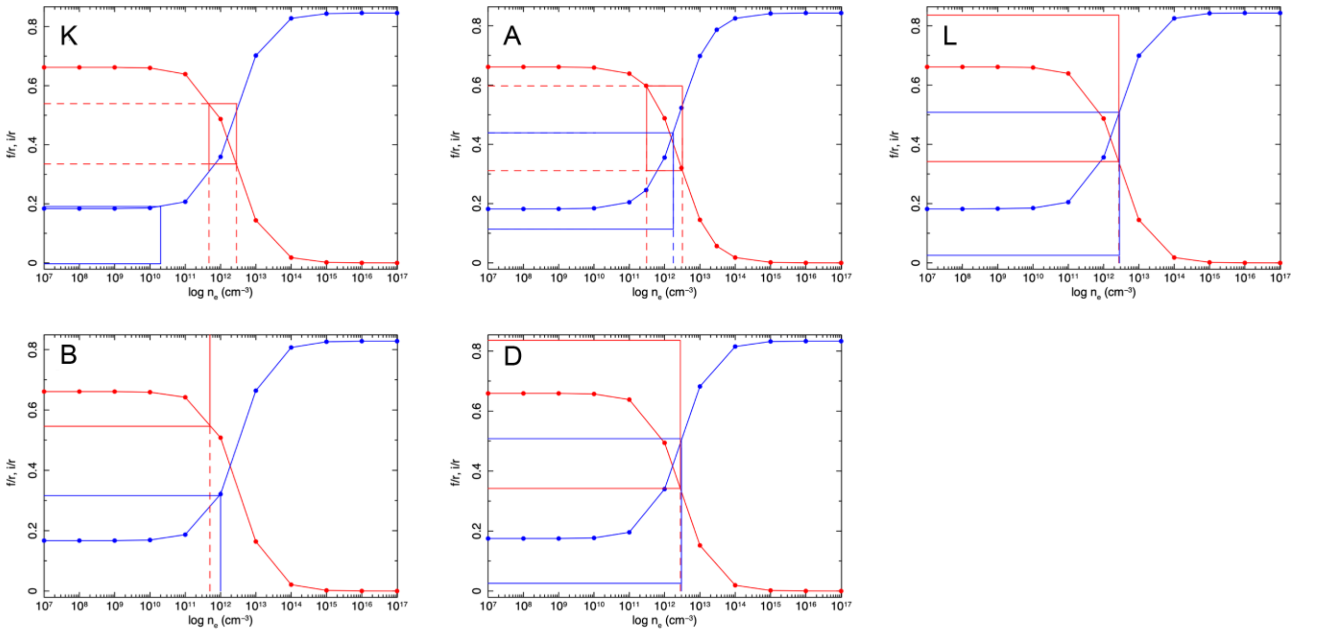

Figure 12. Density diagnosis of the plasma with the intensity ratio of the He-like triplet of Ne at all phases. The indicators are the same as those of Fig. 11. at phase K (0.816), the allowed ranges with *f*/*r* and with *i*/*r* do not overlap. Since the energy resolution is not enough to resolve *i* and *f* and *i* is weak and somewhat broad, we adopt the result with *f*/*r*. Only an upper limit is obtained at phases L (0.935), B (0.968), and D (0.987).

Table 8. The allowed range of the electron number densities n_e in Ne IX at phases K (0.816), A (0.912), L (0.935), B (0.968), and D (0.987). Only the upper limit is determined at all phases but phase K (0.816) and A (0.912).

Phase	n_e (10^{12} cm^{-3})
K (0.816)	0.47–2.83
A (0.912)	0.31–1.76
L (0.935)	< 2.80
B (0.968)	< 1.00
D (0.987)	< 3.00

Table 9. The stellar wind electron number densities of the WR star $n_{e,\,wr}$ and O star $n_{e,\,o}$ (according to equations 1 and 2) at the Ne line-emission site for all phases, using the real distances from the WR star and from the O star (Table 7), respectively, taking the gas element as He. The densities $n_{e,\,wr}$, $n_{e,\,o}$ are much lower than n_e (Table 8).

Phase	$n_{e,\,wr}$ (10^6 cm^{-3})	$n_{e,\,o}$ (10^6 cm^{-3})
K (0.816)	1.2–1.4	0.7–1.1
A (0.912)	3.2–3.6	2.2–3.0
L (0.935)	4.2–4.9	2.5–3.7
B (0.968)	8.1–12.6	3.2–9.8
D (0.987)	41.4–48.6	32.9–52.1

(Pradhan et al. 1981), where f_{ij}, $\pi B(T_r, \nu_{ij})/h\nu_{ij}$ are the oscillator strength and a photon flux of the blackbody radiation from the O star, respectively. T_r is the effective surface temperature of the O star. W is a dilution factor, which represents the geometric reduction due to the decrease in solid angle of the O star. Here, with the radius of the O star R_o and the distance from the center of the O star to the Ne line-emission site D (see Table 7), it is expressed as

$$W = \left(\frac{R_o}{D}\right)^2. \tag{21}$$

Table 10. The result of calculation of the rates of the collisional excitation and photoexcitation and the fraction of the latter to the former at phase K (0.816), A (0.912), L (0.935), B (0.968), and D (0.987).

Phase	$n_e q_{ij}(T_e)$ (s^{-1})	$\Gamma_{ij}(T_r, \nu_{ij})$ (s^{-1})	Fraction (per cent)
K (0.816)	4590–27600	350–750	1.3–16.4
A (0.912)	2960–16800	1030–2120	6.1–71.8
L (0.935)	< 26900	1150–2550	> 4.3
B (0.968)	< 7170	1480–6640	> 20.6
D (0.987)	< 25800	13800–31770	> 53.5

If the relation between the rate of the collisional excitation and that of the photoexcitation is

$$n_e q_{ij}(T_e) \gg \Gamma_{ij}(T_r, \nu_{ij}), \tag{22}$$

then collisional excitation is dominant, and we can adopt the electron densities summarized in Table 8 that are calculated only with the collisional excitation.

The calculation of each term has already been summarized in Itoh et al. (2006). We refer to Martins, Schaerer & Hillier (2005) for the parameters T_r and R_o of the O star. Here, we take into account the uncertainty of T_r and R_o, including the difference between theoretical and observed values.Table 10 shows the result of calculations of the collisional excitation and photoexcitation rates and the fraction of the latter to the former at phase K (0.816), A (0.912), L (0.935), B (0.968), and D (0.987).

Since the fraction of the photoexcitation 1.3–16.4 per cent is moderately small at phase K (0.816), we believe that the value of the resultant electron density ($4.7 \times 10^{11} < n_e < 2.83 \times 10^{12}$ cm^{-3}, see Section 4.2.1) obtained by assuming pure collisional excitation is approximately correct at phase K (0.816). Note, however, that the upper bound of the photoexcitation fraction 16.4 per cent may not be ignored totally; we need to reconsider the photoexcitation effect if the allowed range of the density (a factor of $\sim$6 at this moment) becomes much narrower in the future. Note also that the density upper limit range from the ratio *i*/*r* does not overlap the density range determined from the *f*/*r* ratio at this phase (see Section 4.2.1). However, this is probably because the weak and broad intercombination line is difficult to resolve from the strong resonance line with the limited energy resolution of the RGS.

We also obtained densities of $3.1 \times 10^{11} < n_e < 1.76 \times 10^{12}$ cm^{-3} at phase A (0.912). The photoexcitation fraction amounts to 71.8 per cent at most (Table 10). In this case, we need to evaluate the effect of the photoexcitation on the density measurement much more carefully than at phase K (0.816). The wide range of the fraction (6.1-71.8 per cent, see Table 10) is mainly due to the uncertainties of the measured density as large as a factor of $\sim$6, followed by the uncertainty of R_o^2 in equation (21), which is a factor of $\sim$2, and of the distance squared included in the dilution factor equation (21), which amounts to a factor of 1.6. Further discussion on the effect of the photoexcitation will be made in a forthcoming paper.

4.3 Effects of turbulence and velocity distribution

In the previous section, we utilized the theoretical curve of $|v_{\rm los}|/\sigma_{\rm los}$ to identify the location of the Ne line-emission site, assuming implicitly that the plasma flow is laminar, namely the flow is assumed to follow the geometrical shape of the shock cone. The $\sigma_{\rm los}$ that is obtained from the observation is, however, composed not only of the laminar component but also thermal, turbulent, and the velocity dispersion in the direction perpendicular to the shock cone components, namely

$$\sigma_{\rm obs}^2 = \sigma_{\rm lam}^2 + \sigma_{\rm th}^2 + \sigma_{\rm turb}^2 + \sigma_{\perp}^2, \qquad (23)$$

where the theoretical $\sigma_{\rm los}$ calculated with equation (17) and the observed $\sigma_{\rm los}$ are $\sigma_{\rm lam}$ and $\sigma_{\rm obs}$, respectively. $\sigma_{\rm th}$ is the line-of-sight thermal velocity of Ne which is as small as $\sim$50 km s^{-1} at a plasma temperature of $\sim$0.5 keV. This is smaller than the observed $\sigma_{\rm los}$ by more than an order of magnitude, and hence negligible. On the other hand, since the effect of turbulence $\sigma_{\rm turb}$, and also $\sigma_{\perp}$, which originates from velocity gradient in the direction perpendicular to the shock cone due to a finite shock width, could make significant contribution to the observed $\sigma_{\rm los}$, it is necessary to calculate $v_{\rm los}$ and $\sigma_{\rm los}$ themselves, not $|v_{\rm los}|/\sigma_{\rm los}$, as functions of the distance along the shock cone, in order to identify the Ne line-emission site more precisely. We can get the distances of the emission site from the $v_{\rm los}$ and $\sigma_{\rm los}$ curves independently. Of these two distances, it is expected that the distance from $v_{\rm los}$ provides the true distance, since $\sigma_{\rm los}$ measured from the observed data includes the other components ($\sigma_{\rm turb}^2 + \sigma_{\perp}^2$). We can estimate the velocity dispersion of them from the difference of the two distances, whose analysis will be carried out in a forthcoming paper. Note that the contribution of non-laminar components ($\sigma_{\rm turb}^2 + \sigma_{\perp}^2$) to observed $\sigma_{\rm los}$ does not affect the density evaluation of the plasma emitting the Ne lines, since the location of the Ne line-emission site should be farther away from the O star than the estimation made in this paper.

5 CONCLUSION

In this paper we present the results of our analysis the *XMM–Newton* RGS data taken during 2008 May through 2016 June that cover one entire orbit of WR140, in order to carry out diagnosis of the plasma formed through collision of the stellar winds emanating from the two component stars. We find that the X-rays in the band 0.5-2.5 keV are detected only during the orbital phases when the O star is in front of the WR star, and at such phases, we obtained the line-of-sight velocity $v_{\rm los}$ and its dispersion $\sigma_{\rm los}$ of Ne line-emission plasma to be between -600 to -1200 km s^{-1} and 400–700 km s^{-1}, respectively. From the spectral fits to the He-like and H-like Ne Kα lines, the temperature of the Ne line-emission plasma is found to be in the range 0.4–0.8 keV. Since plasma producing highly ionized Kα emission lines of Ne is moving along the shock cone formed through collision of the stellar winds, we calculated the shape of the shock cone under the condition of pressure balance perpendicular to the cone. Assuming that the plasma flow is laminar and follows the shock cone, from the orbital variation of the line-of-sight velocity and dispersion of the Ne lines, we found that the Ne line-emission site is located at a distance of (0.9–8.9) $\times$ 10^{13} cm from the stagnation point of the shock at phases K (0.816), A (0.912), L (0.935), B (0.968), and D (0.987) (Table 7). We also found that the plasma electron density there at phase K (0.816) is (0.47-2.83)$\times$ 10^{12} cm^{-3}, which is obtained from the intensity ratio of *f*/*r* of the He-like Ne triplet. Based on the location of the Ne line-emission site on the shock cone, the contribution of the photoexcitation from ^{3}S$_1$ level to ^{3}P$_{2,\,1}$ level is obtained to be 1.3–16.4 per cent of the collisional excitation at phase K (0.816). The 16.4 per cent photoexcitation contribution is not totally negligible. We need to take this into account for more accurate estimates of electron number density. Although we find a finite value of the electron number density (0.31-1.76)$\times$ 10^{12} cm^{-3} considering solely collisional excitation also at phase A (0.912), the rate of the photoexcitation amounts to 71.8 per cent at most. This implies we need to estimate the effect of the photoexcitation carefully at this phase.

In summary, we show that the temperature and the density of the Ne line-emission-site of the plasma can be evaluated with the intensity ratio of the He-like and H-like Kα lines, and the ratios *f*/*r* and *i*/*r* of the He-like triplet, respectively. In addition, from the ratio $|v_{\rm los}|/\sigma_{\rm los}$, we can identify the mean location of the Ne line-emission site. By doing the same thing with other emission lines, we can deduce the profile of the temperature and the density of the plasma along the shock cone, possibly with O- Kα lines and Fe-L lines with the current RGS data (Fig. 3), and with other lines up to Fe-K with high-resolution spectrometers in the future.

ACKNOWLEDGEMENTS

The material is based upon work supported by NASA under award number 80GSFC21M0002. KH is supported by the NASA grants 15-NUSTAR215-0026, 80NSSC19K0690, JPL grant 001287-00001. This research made use of the Astrophysics Data System and the HEASARC archive. This research was partially supported by the Ministry of Education, Culture, Sports, Science and Technology (MEXT), Grant-in-Aid Nos.19K21886 and 20H00175. AFJM is grateful for financial aid from NSERC (Canada). CMPR acknowledges support from the National Science Foundation under Grant No. AST-1747658. The authors are grateful to Dr. Ian Stevens for a number of his useful comments.

DATA AVAILABILITY

The data that support the findings of this study are available in the *XMM−Newton* science archive at http://nxsa.esac.esa.int/nxsa-web/#home, reference number 0555470701, 0555470801, 0555470901, 0555471001, 0555471101, 0555471201, 0651300301, 0651300401,

0762910301, 0784130301. These data were reduced and analyzed with the following resources available in the public domain: XSPEC, which is part of HEASOFT (https://heasarc.gsfc.nasa.gov/docs/software/lheasoft/), SAS (https://www.cosmos.esa.int/web/xmm-newton/sas) and AtomDB (http://www.atomdb.org/index.php).

REFERENCES

Anders E., Grevesse N., 1989, Geochim. Cosmochim. Acta, 53, 197

Arnaud K. A., 1996, in Jacoby G. H., Barnes J., eds, ASP Conf. Ser. Vol. 101, Astronomical Data Analysis Software and Systems V. Astron. Soc. Pac., San Francisco. p. 17

Cantó J., Raga A. C., Wilkin F. P., 1996, ApJ, 469, 729

De Becker M., Pittard J. M., Williams P., Consortium WR140, 2011, Bull. Soc. R. Sci. Liege, 80, 653

den Herder J. W. et al., 2001, A&A, 365, L7

Fahed R. et al., 2011, MNRAS, 418, 2

Gabriel A. H., Jordan C., 1969, MNRAS, 145, 241

Itoh K., Okada S., Ishida M., Kunieda H., 2006, ApJ, 639, 397

Jansen F. et al., 2001, A&A, 365, L1

Koyama K., Kawada M., Takano S., Ikeuchi S., 1990, Publ. Astron. Soc. Japan, 42, L1

Koyama K., Maeda Y., Tsuru T., Nagase F., Skinner S., 1994, Publ. Astron. Soc. Japan, 46, L93

Lépine S., Moffat A. F. J., 1999, ApJ, 514, 909

Martins F., Schaerer D., Hillier D. J., 2005, A&A, 436, 1049

Masai K., 1984, Ap&SS, 98, 367

Monnier J. D. et al., 2011, ApJ, 742, L1

Pittard J. M., 2007, ApJ, 660, L141

Pittard J. M., Dougherty S. M., 2006, MNRAS, 372, 801

Pittard J. M., Stevens I. R., 1997, MNRAS, 292, 298

Pollock A. M. T., Corcoran M. F., Stevens I. R., Williams P. M., 2005, ApJ, 629, 482

Pollock A. M. T. et al., 2021, ApJ, 923, 191

Porquet D., Mewe R., Dubau J., Raassen A. J. J., Kaastra J. S., 2001, A&A, 376, 1113

Pradhan A. K., Shull J. M., 1981, ApJ, 249, 821

Pradhan A. K., Norcross D. W., Hummer D. G., 1981, ApJ, 246, 1031

Puls J. et al., 1996, A&A, 305, 171

Setia Gunawan D. Y. A., van der Hucht K. A., Williams P. M., Henrichs H. F., Kaper L., Stickland D. J., Wamsteker W., 2001, A&A, 376, 460

Stevens I. R., Blondin J. M., Pollock A. M. T., 1992, ApJ, 386, 265

Sugawara Y. et al., 2015, Publ. Astron. Soc. Japan, 67, 121

Thomas J. D. et al., 2021, MNRAS, 504, 5221

Usov V. V., 1992, ApJ, 389, 635

Williams P. M., van der Hucht K. A., Pollock A. M. T., Florkowski D. R., van der Woerd H., Wamsteker W. M., 1990, MNRAS, 243, 662

Williams P. M. et al., 2009, MNRAS, 395, 1749

Zhekov S. A., Skinner S. L., 2000, ApJ, 538, 808

APPENDIX A: DERIVING EQ. 8

In this section, we show the process of deriving equation (8) from equation (7) in the main text.

The ram pressure of the WR star $\boldsymbol{P}_{\rm wr}$ and that of the O star $\boldsymbol{P}_{\rm o}$ are as follows:

$$\begin{aligned}\boldsymbol{P}_{\rm wr}(r_{\rm wr}) &= \rho_{\rm wr}(r_{\rm wr})v_{\rm wr}^2(r_{\rm wr})\,\hat{\boldsymbol{r}}_{\rm wr}\\ &= \frac{\dot{M}_{\rm wr}v_{\infty,\rm wr}}{4\pi r_{\rm wr}^2}\left(1-\frac{R_{\rm wr}}{r_{\rm wr}}\right)\hat{\boldsymbol{r}}_{\rm wr},\end{aligned} \quad \text{(A1)}$$

$$\boldsymbol{P}_{\rm o}(r_{\rm o}) = \rho_{\rm o}(r_{\rm o})v_{\rm o}^2(r_{\rm o})\,\hat{\boldsymbol{r}}_{\rm o} = \frac{\dot{M}_{\rm o}v_{\infty,\rm o}}{4\pi r_{\rm o}^2}\left(1-\frac{R_{\rm o}}{r_{\rm o}}\right)\hat{\boldsymbol{r}}_{\rm o}, \quad \text{(A2)}$$

where $\hat{\boldsymbol{r}}_{\rm wr}$ and $\hat{\boldsymbol{r}}_{\rm o}$ are the unit vectors of the stellar wind direction of each star, which can be written as

$$\hat{\boldsymbol{r}}_{\rm wr} = \frac{\boldsymbol{r}_{\rm wr}}{|\boldsymbol{r}_{\rm wr}|} = \frac{\boldsymbol{r}_{\rm wr}}{r_{\rm wr}},\quad \hat{\boldsymbol{r}}_{\rm o} = \frac{\boldsymbol{r}_{\rm o}}{|\boldsymbol{r}_{\rm o}|} = \frac{\boldsymbol{r}_{\rm o}}{r_{\rm o}}. \quad \text{(A3)}$$

In the scheme of Fig. 7, they can be written as

$$\begin{aligned}\hat{\boldsymbol{r}}_{\rm wr} &= \frac{1}{r_{\rm wr}}\left(x+\frac{1}{1+\varphi}d,\ y\right)\\ &= \frac{1}{\sqrt{\left(x+\frac{1}{1+\varphi}d\right)^2+y^2}}\left(x+\frac{1}{1+\varphi}d,\ y\right).\end{aligned} \quad \text{(A4)}$$

$$\begin{aligned}\hat{\boldsymbol{r}}_{\rm o} &= \frac{1}{r_{\rm o}}\left(x-\frac{\varphi}{1+\varphi}d,\ y\right)\\ &= \frac{1}{\sqrt{\left(x-\frac{\varphi}{1+\varphi}d\right)^2+y^2}}\left(x-\frac{\varphi}{1+\varphi}d,\ y\right).\end{aligned} \quad \text{(A5)}$$

The unit vectors in the normal direction, $\boldsymbol{n}_{\rm wr}$ and $\boldsymbol{n}_{\rm o}$, can be written as follows.

$$\begin{aligned}\boldsymbol{n}_{\rm wr} &= \frac{1}{\sqrt{(\mathrm{d}x)^2+(\mathrm{d}y)^2}}(\mathrm{d}y,\ -\mathrm{d}x)\\ &= \frac{1}{\sqrt{\left(\frac{\mathrm{d}x}{\mathrm{d}y}\right)^2+1}}\left(\frac{\mathrm{d}x}{\mathrm{d}y},\ -1\right)\end{aligned} \quad \text{(A6)}$$

$$\begin{aligned}\boldsymbol{n}_{\rm o} &= \frac{1}{\sqrt{(\mathrm{d}x)^2+(\mathrm{d}y)^2}}(-\mathrm{d}y,\ \mathrm{d}x)\\ &= \frac{1}{\sqrt{\left(\frac{\mathrm{d}x}{\mathrm{d}y}\right)^2+1}}\left(-\frac{\mathrm{d}x}{\mathrm{d}y},\ 1\right) = -\boldsymbol{n}_{\rm wr}.\end{aligned} \quad \text{(A7)}$$

Using these, equation (7) can finally be written as follows:

$$\frac{\mathrm{d}x}{\mathrm{d}y} = \frac{1}{y}\left\{x + \frac{\frac{1}{r_{\rm wr}^3}\left(1-\frac{R_{\rm wr}}{r_{\rm wr}}\right) - \frac{\varphi^3}{r_{\rm o}^3}\left(1-\frac{R_{\rm o}}{r_{\rm o}}\right)}{\frac{1}{r_{\rm wr}^3}\left(1-\frac{R_{\rm wr}}{r_{\rm wr}}\right) + \frac{\varphi^2}{r_{\rm o}^3}\left(1-\frac{R_{\rm o}}{r_{\rm o}}\right)}\frac{d}{1+\varphi}\right\}. \quad \text{(A8)}$$

We obtain equation (8) in the main text by normalizing x, y, and the distances $r_{\rm wr}$ and $r_{\rm o}$, and the radii $R_{\rm wr}$ and $R_{\rm o}$ with the separation of the component stars d as in equation (9) of the main text.

This paper has been typeset from a TEX/LATEX file prepared by the author.